applied sciences

MDPI

Article

Utilizing MicroGenetic Algorithm for Optimal Design of Permanent-Magnet-Assisted WFSM for Traction Machines

Han-Soo Seo [1], Chan-Bae Park [1], Seong-Hwi Kim [2], Gang Lei [3], Youguang Guo [3] and Hyung-Woo Lee [1,*]

[1] Department of Railway Vehicle & Operation System Engineering, Korea National University of Transportation, 157, Cheoldobangmulgwan-ro, Uiwang-si 16106, Republic of Korea; shs1513@naver.com (H.-S.S.); cbpark@ut.ac.kr (C.-B.P.)
[2] Department of Electronic Engineering, Hanyang University, 222, Wangsimni-ro, Seongdong-gu, Seoul 04763, Republic of Korea; nyen0578@naver.com
[3] School of Electrical and Data Engineering, University of Technology Sydney, 15, Broadway, Ultimo, NSW 2007, Australia
* Correspondence: krhwlee@ut.ac.kr

Abstract: With increasing worries about the environment, there is a rising focus on saving energy in various industries. In the e-mobility industry of electric motors, permanent magnet synchronous motors (PMSMs) are widely utilized for saving energy due to their high-efficiency motor technologies. However, challenges like environmental degradation from rare earth development and difficulties in controlling magnetic field fluctuations persist. To address these issues, active research focuses on the wound field synchronous motor (WFSM), known for its ability to regulate field current efficiently across various speeds and operating conditions. Nevertheless, compared with other synchronous motors, the WFSM tends to exhibit relatively lower efficiency and torque density. Because the WFSM involves winding both the rotor and the stator, it results in increased copper and iron losses. In this article, a model that enhances torque density by inserting permanent magnets (PMs) into the rotor of the basic WFSM is proposed. This proposed model bolsters the d axis magnetic flux, thereby enhancing the motor's overall performance while addressing environmental concerns related to rare-earth materials and potentially reducing manufacturing costs when compared with those of the PMSM. The research methodology involves a comprehensive sensitivity analysis to identify key design variables, followed by sampling using optimal Latin hypercube design (OLHD). A surrogate model is then constructed using the kriging interpolation technique, and the optimization process employs a micro-genetic algorithm (MGA) to derive the optimal model configuration. The algorithm was performed to minimize the use of PMs when the same torque as that of the basic WFSM is present, and to reduce torque ripple. Error assessment is conducted through comparisons with finite element method (FEM) simulations. The optimized permanent-magnet-assisted WFSM (PMa-WFSM) model improved efficiency by 1.08% when it was the same size as the basic WFSM, and the torque ripple decreased by 5.43%. The proposed PMa-WFSM derived from this article is expected to be suitable for use in the e-mobility industry as a replacement for PMSM.

Keywords: wound field synchronous motor (WFSM); permanent-magnet-assisted (PMa); optimal Latin hypercube design (OLHD); surrogate model; micro-genetic algorithm (MGA)

Citation: Seo, H.-S.; Park, C.-B.; Kim, S.-H.; Lei, G.; Guo, Y.; Lee, H.-W. Utilizing MicroGenetic Algorithm for Optimal Design of Permanent-Magnet-Assisted WFSM for Traction Machines. *Appl. Sci.* **2024**, *14*, 5150. https://doi.org/10.3390/app14125150

Academic Editor: Adel Razek

Received: 25 April 2024
Revised: 3 June 2024
Accepted: 5 June 2024
Published: 13 June 2024

1. Introduction

In recent years, spurred by escalating environmental concerns, there has been a notable surge in development efforts within the e-mobility industry, particularly focusing on the creation of electric motors boasting high efficiency and output [1–3]. Various motors find application in industrial settings, including the induction motor (IM), synchronous reluctance motor (SynRM), permanent-magnet synchronous motor (PMSM), and wound field synchronous motor (WFSM) [4–7]. Among these options, rare-earth PM motors

are often preferred due to their relatively high power density and suitability for high-speed operations, especially in the case of PMSM [8]. Consequently, rare-earth PM motors have emerged as the dominant choice in contemporary industrial settings [9]. However, challenges such as high costs, the unstable supply chain of rare-earth materials, and complexities in controlling weak field regions have heightened interest in alternative solutions like the WFSM [10]. The WFSM offers an advantage by enabling the direct manipulation of the field current through the winding of field coils with the DC current, facilitating a broad operating range and high efficiency in high-speed area [11,12]. Especially for traction application, it is crucial to meet the torque and speed requirements. Up to the rated speed, a consistent rated torque must be maintained, and as the speed increases, the torque should decrease to maintain a constant output [13]. To achieve the same output as a PMSM, the WFSM must be designed accordingly, necessitating a focus on achieving high power density. In the case of WFSM, a significant challenge arises with high current densities, leading to rotor core saturation. This phenomenon introduces nonlinear variations in output performance and torque, exacerbating concerns about temperature rise. Therefore, meticulous attention to the number of coil turns and the selection of rotor current is crucial for high power density [14,15]. Furthermore, considering the inherent presence of reluctance torque in the WFSM, it is essential to account for both the d axis inductance and the q axis inductance. The process involves winding coils around the rotor to generate magnetic flux, resulting in the d axis inductance (L_d) having higher magnetic resistance compared with the q axis inductance (L_q) [10]. Calculating the inductance of each axis plays a crucial role in evaluation and design for such torque.

Before proceeding with the design and production of the WFSM for practical applications in railway vehicle traction, a preliminary assessment was conducted using a downscaled version of the WFSM rated at 5 kW. When designing a 5 kW WFSM, it is essential to design it to meet the torque–speed (T-N) curve shown in Figure 1.

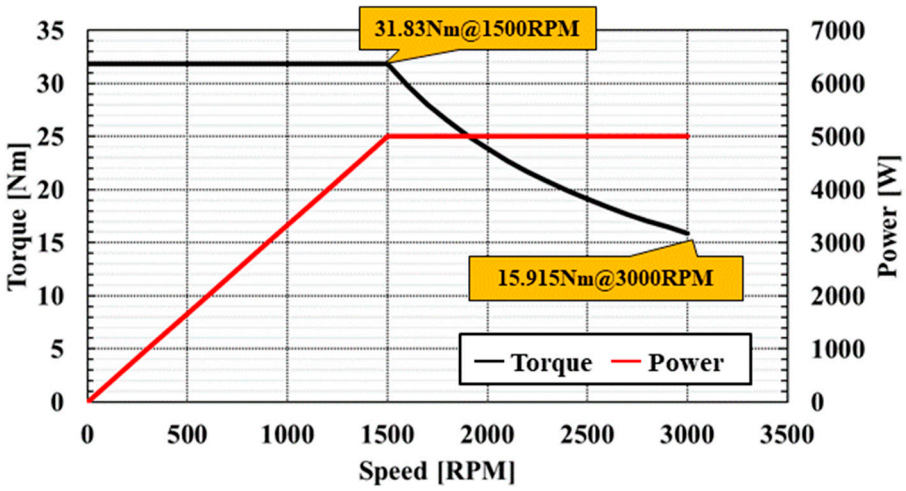

Figure 1. Torque and speed curve requirement for 5 kW Traction motor.

The basic WFSM configuration is as shown in Figure 2a. This experimental setup allowed for an initial evaluation of the motor performance. The rated speed was set at 1500 RPM, with a corresponding torque requirement of 31.83 Nm to achieve the desired 5 kW output. And basic WFSM model calculated the output performance through FEM modeling and compared it with the experimental value.

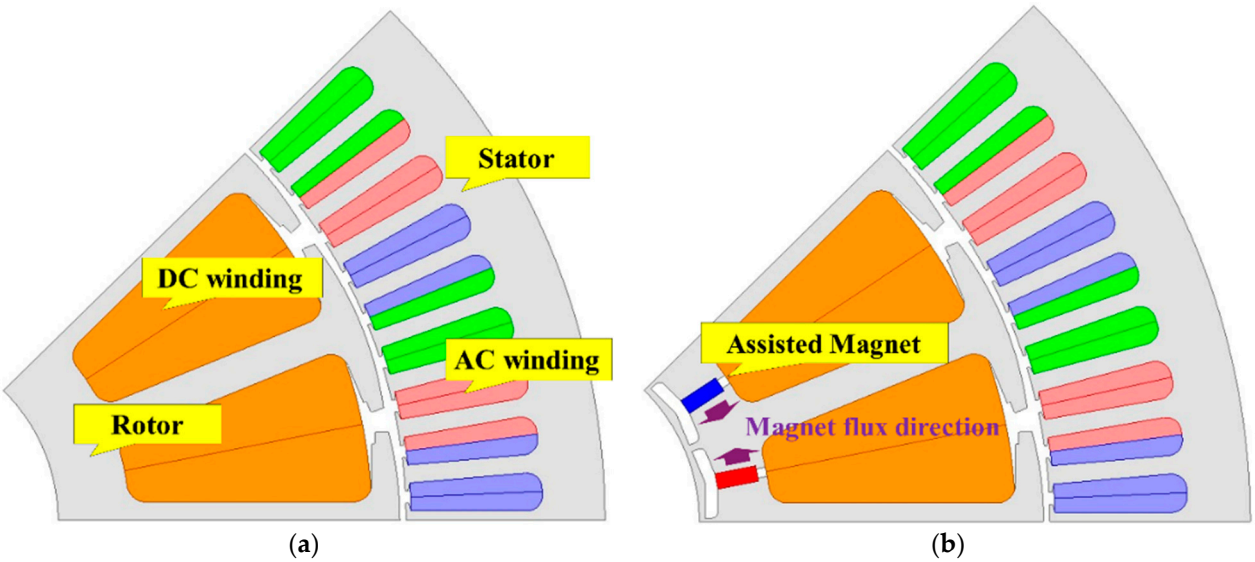

Figure 2. Structure of machines: (**a**) basic WFSM; (**b**) PMa-WFSM.

This article introduces a PMa-WFSM aimed at enhancing d axis flux by incorporating permanent magnets, as depicted in Figure 2b. Specifically, neodymium permanent magnets are strategically inserted into the rotor yoke to bolster magnetic flux. To formulate an optimization model, sensitivity analysis was initially conducted to identify key design variables with significant impacts on torque. Subsequently, sampling was carried out using the OLHD methodology to ensure a well-distributed selection of design variables across the parameter space. Moreover, in pursuit of cost-effectiveness, the optimization design process leveraged the MGA to minimize the utilization of permanent magnets while maximizing overall efficiency and reducing torque ripple. The electromagnetic characteristics of the proposed design were calculated through 2D FEM analysis [16].

2. Specification and Experiment of Basic WFSM

A typical WFSM has a saliency ratio (L_q/L_d), and this ratio contributes to the generation of reluctance torque (T_r). The output torque (T) of the motor comprises two main components: magnetic torque (T_m) and reluctance torque. The former arises from the alignment of the magnetic flux generated by the stator winding with that produced by the rotor winding. On the other hand, reluctance torque is a result of the disparity between L_d and L_q of the rotor. This phenomenon is fundamental in understanding the torque equation of the conventional WFSM. In Equation (1), p is the number of pole pairs, Ψ_f is the field flux, i_a is the peak value of the stator current, and β is the current phase angle [17].

$$T = T_r + T_m = 1.5p\{\Psi_f i_a \cos\beta + 0.5(L_q - L_d){i_a}^2 \sin 2\beta\} \quad (1)$$

To calculate the inductance using the torque equation, the magnetic equivalent circuit is represented as shown in Figure 3. The magnetic resistance can be calculated as follows:

$$R_m = \frac{l}{\mu A} \quad (2)$$

where l is the length, μ is the permeability, and A is the cross-sectional area of the magnetic flux path. The relative permeability of air and copper is significantly smaller compared with that of the core, indicating that the magnetic resistance of the d axis is smaller than

that of the q axis, as expressed in the equation. With the magnetic resistance determined, the inductance can be calculated as follows:

$$L_d = \frac{NF_d}{i_d} = \frac{N^2}{R_{gd} + R_{sd} + R_{rd}}, \; L_q = \frac{NF_q}{i_q} = \frac{N^2}{R_{gq} + R_{sq} + R_{rq}} \tag{3}$$

where F_d, i_d, R_{gd}, R_{sd}, and R_{rd} are components of the d axis, which includes the magnetic flux, current, air–gap reluctance, stator magnetic resistance, and rotor magnetic resistance; F_q, i_q, R_{gq}, R_{sq}, and R_{rq} are components of the q axis, which includes the magnetic flux, current, air–gap magnetic resistance, stator magnetic resistance, and rotor magnetic resistance. N represents a turn of the winding coil.

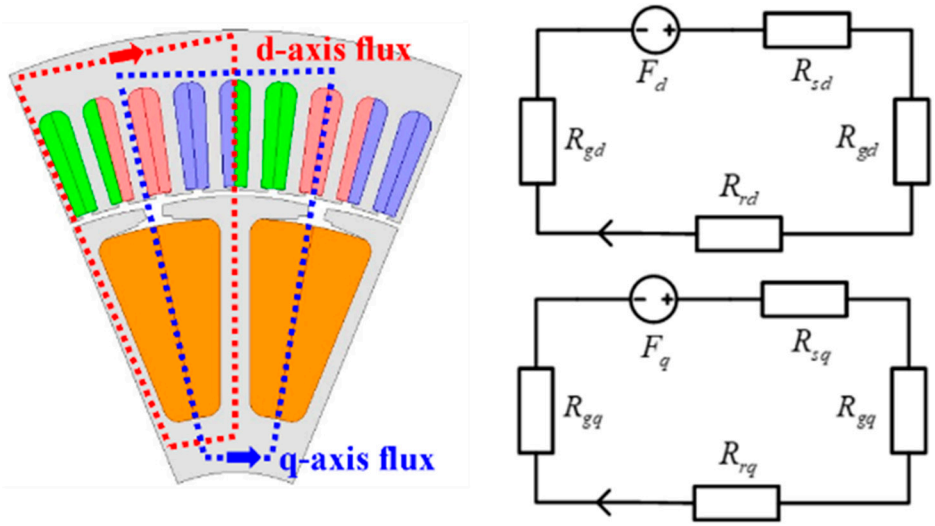

Figure 3. The magnetic equivalent circuit of the basic WFSM.

The specifications of the basic WFSM are shown in Table 1. To achieve rated torque, the rated stator current was selected to be 13.5 A_{rms}, and the rotor current was chosen to be 5 A_{dc}. Additionally, considering the current density to be below 4 A/mm^2 and manufacturing constraints, a slot fill factor of 0.35 was adopted, with the number of turns for the stator being set to six turns, while for the rotor, it was set to six turns. The winding method for the stator used distributed winding to reduce harmonics, while the rotor was wound with concentrated windings. The number of poles per phase is three. After selecting the specifications, the design process was initiated, and a 5 kW WFSM was manufactured. The experimental setup was configured as shown in Figure 4a. The average torque value was extracted using a servo motor. The difference between the experimental values and FEM analysis results in output performance was compared through the no-load EMF peak, no-load EMF plot, and average torque.

Table 1. Specification of basic WFSM.

Specification	Value
Output power	5 kW
Rated torque/speed	31.91 Nm/1500 rpm
Rated stator peak current	19.09 A
Rated rotor current	5 A_{dc}
Number of poles/slots	16 pole/72 slot
Stator/rotor outer diameter	236 mm/170 mm
Coil space factor	0.35

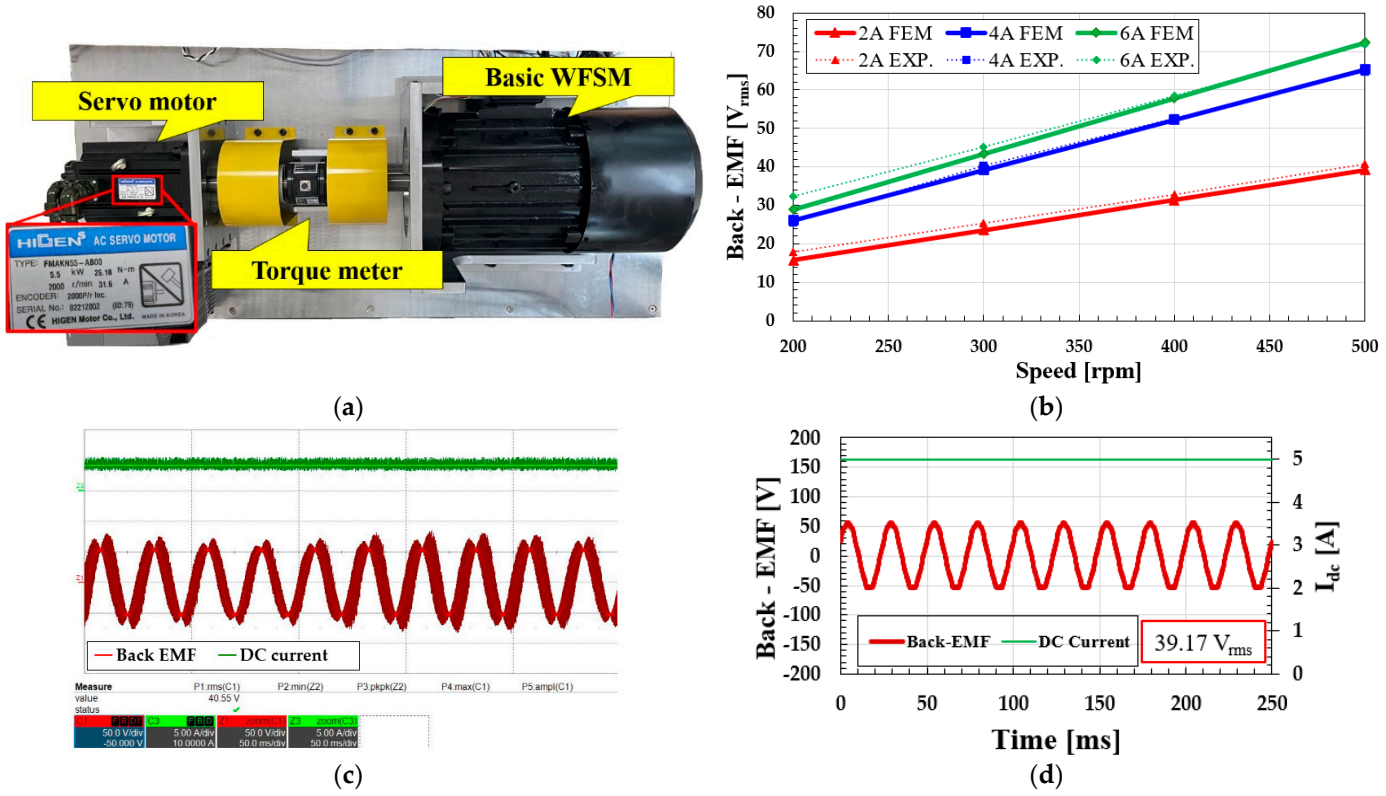

Figure 4. WFMS experiment procedure: (**a**) experimental environment; (**b**) variation in field current with rotation speed; (**c**) no-load EMF experimental waveform (300 rpm, I_{dc} = 4 A); (**d**) no-load EMF FEM waveform (300 rpm, I_{dc} = 4 A).

The output performance of a WFSM is significantly influenced by the field current. To comprehensively investigate this influence, experimental trials were meticulously conducted, systematically varying the rotor current (I_{dc}) across three discrete levels: 2 A, 4 A, and 6 A. Additionally, the rotational speed was varied from 200 rpm to 500 rpm in precise 100 rpm increments. Under no-load conditions, a fundamental observation was the proportional increase in the root mean square (V_{rms}) of the no-load back electromotive force (EMF) with both the rotor current and the rotational speed. Under lower-rotor-current conditions, the motor core exhibited minimal saturation, resulting in a negligible discrepancy between analytical predictions and measured values. However, as the rotor current was progressively increased, the motor core approached saturation, leading to nonlinearity in the back EMF characteristics. Consequently, this nonlinear behavior contributed to a corresponding increase in the error between the FEM analysis results and the measured values. In the low-speed range, the influence of noise is relatively significant, resulting in larger errors. However, as the motor speed transitions to higher speeds, the errors gradually decrease. This trend suggests that the system becomes more stable and predictable at higher speeds, leading to more accurate predictions and mitigating the impact of noise.

During the load testing phase, the electric motor was energized and the average torque was derived by capturing internal torque commands communicated from the servo motor. This methodically involved incrementally adjusting the armature current, varying it from 1.5 A to 9.5 A in 4 A increments, to enable a thorough comparison between experimental findings and FEM analysis outcomes across multiple data points.

Despite grappling with challenges such as core saturation and nonlinear behavior, the comprehensive analysis yielded invaluable insights. The deviation was derived by comparing the FEM analysis results of the motor with experimental values, thereby verifying the credibility of the computational results. The error between the FEM analysis results and the experimental data was calculated. For the EMF, the experimental value measured was

40.55 V_{rms}, while the FEM analysis calculated 39.17 V_{rms}. An error of 3.5% was attributed to noise during the experimental measurement process. The comparison results of the torque average, depicted in Figure 5, reveal an overall deviation of 8.15% between the experimental measurements and the FEM analysis results. This finding underscores the reliability of the analysis and the low discrepancy observed, reaffirming the credibility of the experimental methodology and the analytical framework employed.

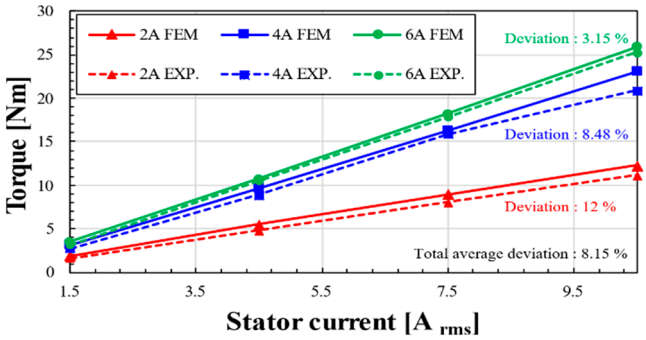

Figure 5. Comparison of experimental and FEM analysis torque values.

3. Design of PMa-WFSM

The proposed topology presented in this article involves integrating assisted permanent magnets into the rotor yoke to augment the magnetic flux along the d axis direction and bolster the magnetic torque. One aspect worth exploring further is the impact of different permanent magnet materials on the overall performance of the motor. The selection of materials for these permanent magnets includes ferrite, neodymium, and samarium–cobalt. Ferrite permanent magnets are notably economical but exhibit lower coercivity and magnetic flux density compared with other materials. Table 2 shows the properties of the magnets. Therefore, when employed as assisted magnets, they may enhance the magnetic flux along the d axis while concurrently elevating magnetic resistance, thereby potentially leading to a reduction in torque. On the other hand, samarium–cobalt permanent magnets offer the advantage of possessing a high knee point and robust temperature stability, rendering them less susceptible to irreversible demagnetization. However, they are comparatively pricier than neodymium magnets and demonstrate lower remanence and magnetic flux density. As a result, the neodymium magnet (N42) made by ARNOLD location in New York, which provides a balanced combination of cost-effectiveness, high coercivity, and magnetic flux density, was deemed suitable for the intended application.

Table 2. Specification of permanent magnet.

Name	Value			
	BR [T]	BH max. [kJ/m^3]	HCB min. [kA/m]	TEMP max. [°C]
Ferrite magnet (Y20) [ARNOLD]	0.2	18	135	250
Samarium–cobalt magnet (24HE) [ARNOLD]	1.02	195	765	350
Neodymium magnet (N42) [ARNOLD]	1.315	334	955	80

The torque equation for the PMa-WFSM is calculated by adding the magnetic flux linkage (Ψ_m) of the permanent magnets to the magnetic torque term of Equation (1).

$$T=T_r + T_m=1.5p\{(\Psi_f + \Psi_m)i_a\cos\beta + 0.5(L_q - L_d)i_a{}^2\sin 2\beta\} \quad (4)$$

Due to the addition of permanent magnets, there is a change in inductance, requiring recalculations. Figure 6 represents the magnetic equivalent circuit of the proposed model. Additionally, the addition of permanent magnets results in changes to the inductance,

necessitating a recalculation. F_{pm} is permanent magnet flux, R_{pmd} and R_{pmq} represent the permanent magnet reluctances of the d axis and q axis components.

$$L_d = \frac{N(F_d + F_{pm})}{i_d} = \frac{N^2}{R_{gd} + R_{sd} + R_{rd} + R_{pmd}}, \; L_q = \frac{NF_q}{i_q} = \frac{N^2}{R_{gq} + R_{sq} + R_{rq} + R_{mq} + R_{pmq}} \tag{5}$$

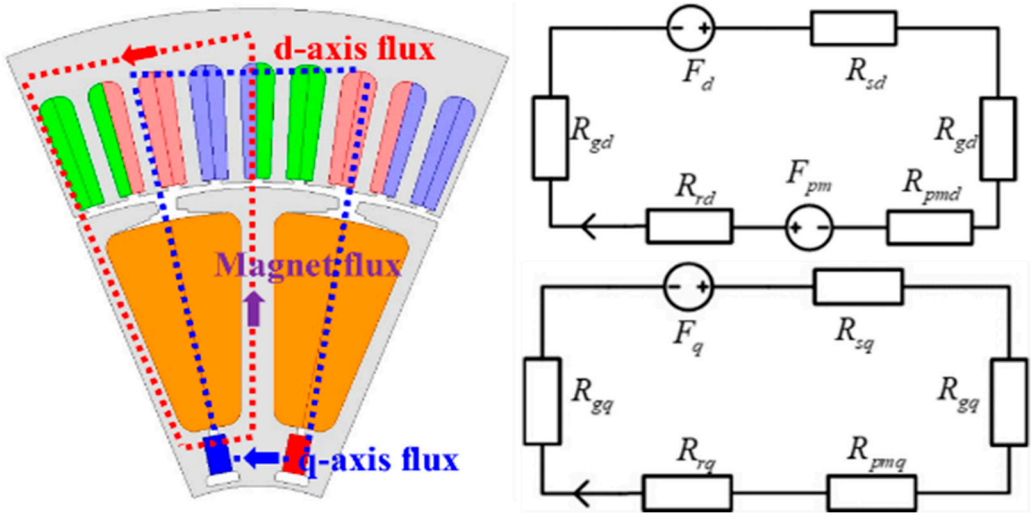

Figure 6. The magnetic equivalent circuit of the PMa-WFSM.

Using a magnetic equivalent circuit, inductance variation and torque were calculated, and based on this, FEM analysis was performed using the fixed permeability method. First, the torque of the PMa-WFSM was classified into three categories as shown in Figure 7. The reluctance torque due to the inductance difference was derived by applying only the stator current, the magnetic torque (winding) was derived via the DC current supply only to the rotor winding, and the magnetic torque (magnet) was derived by inserting only the permanent magnet without any current supply. The sum of the three torque components yields the total torque, with the maximum torque occurring at a current phase angle of 15 degrees [18].

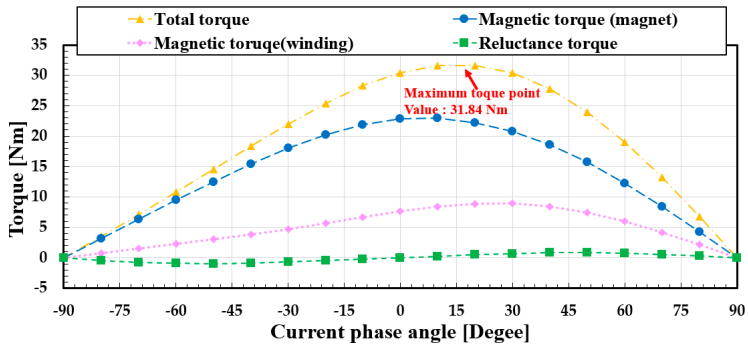

Figure 7. Torque components of WFSM and PMa-WFSM.

Additionally, a reduction in I_{dc} is required due to the saturation of the rotor teeth. With the addition of permanent magnets, as demonstrated in Figure 8, saturation of the rotor teeth occurs. Therefore, to prevent non-linear output performance, I_{dc} was adjusted to 3.5 A_{dc}. The arrangement of the permanent magnets with barriers on the shaft side serves to enhance the magnetic field concentration in the core region, thereby optimizing motor performance. The selected core starts to exhibit nonlinear saturation at 1.8 T, so the maximum saturation point of the model was adjusted to 1.73 T. Additionally, it was

confirmed through the flux line distribution that the flux generated by the permanent magnet and the flux generated by the windings combine in the rotor teeth and permeate through to the stator. This configuration not only improves the efficiency of the motor but also ensures stable operation under varying load conditions. Furthermore, by adjusting I_{dc} to mitigate saturation effects, the motor output characteristics can be finely tuned to meet specific application requirements. These combined design considerations contribute to the overall enhancement of the PMa-WFSM performance and reliability.

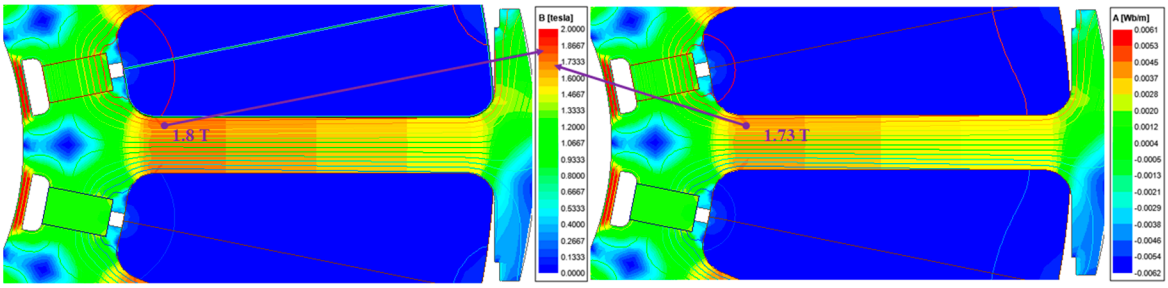

(**a**) (**b**)

Figure 8. The flux density of the PMa-WFSM: (**a**) I_{dc} = 5 A; (**b**) I_{dc} = 3.5 A.

4. Optimal Design Process

The design process followed the parameters of the basic WFSM, maintaining consistency in the stator's outer diameter and other design variables. However, only the parameters related to the assisted magnet were considered design variables in this study. Moreover, to achieve comparable output performance, an equality constraint aiming for a rated torque of 32 Nm was established. To ensure optimal performance, a constraint was implemented to keep the torque ripple below 6%. Furthermore, in line with cost-effectiveness and resource conservation objectives, the optimization objective function aimed to minimize the cross-sectional area of the permanent magnets.

In total, eight design variables were selected, taking into account feasibility. Their respective contributions to the alterations in output performance were thoroughly evaluated through sensitivity analysis. The main variables are marked with yellow boxes in the table to the right of Figure 9. Subsequently, based on the results of this analysis, four major design variables, which exhibited substantial impacts on torque and torque ripple, were further refined and chosen for subsequent optimization, as shown in Figure 10.

To ensure optimal projective properties and space filling across the designated design range, a sampling approach utilizing OLHD was employed. Initially, a comprehensive set of 80 sampling points was strategically chosen, a number calculated based on the inclusion of four essential design variables. These training data points were designated for use in data learning purposes, and their number was selected to be 80, where nTR represents the number of training data points and nDV denotes the number of design variables [19].

$$nTR > 1.5(nDV\ +1)(nDV\ +2)/2 \tag{6}$$

The initial 80 training points were calculated using FEM analysis, and a surrogate model was generated based on these data. To generate a surrogate model, two primary types of methods are available: one is regression methods and the other is interpolation methods. Interpolation methods unlike regression methods do not rely on correlation coefficients to predict distributed training data. Instead, interpolation techniques like kriging offer a continuous and smooth estimation of the underlying function throughout the entire design space. This detailed estimation fosters a deeper understanding of the relationship between input variables and output performance. Furthermore, interpolation enables the estimation of output performance at any point within the design domain, even in cases where training data points are scarce or absent. This versatility enhances the applicability of the surrogate model, particularly in situations where exhaustive experimental testing

is impractical or overly costly. Unlike regression, interpolation does not introduce errors between experimental data and predicted values, as it relies solely on the spatial distance between each data point. To quantify the error between the FEM calculation results and the predicted values, 9 test points, which represent approximately 10% of the 80 training data points, were selected, where nTE represents the number of test points. The error between the training points and FEM analysis results was then computed using the root mean square error (RMSE), where $y_1(X_i)$ is the value of the FEM analysis results and $y_2(X_i)$ is the value of the surrogate model.

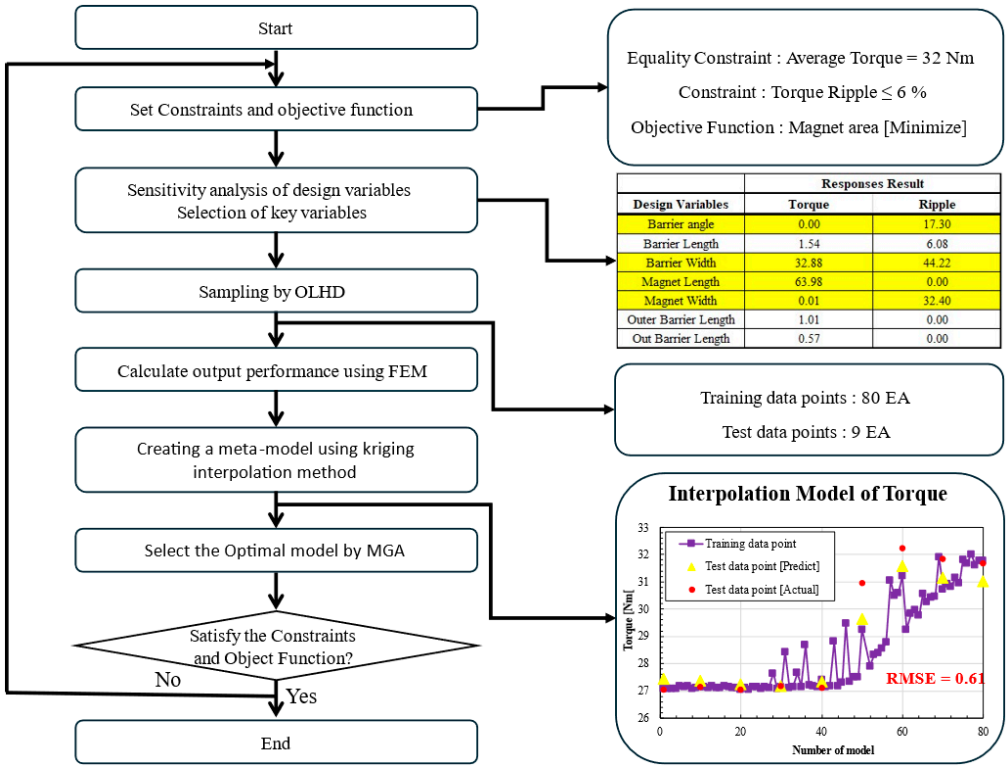

Figure 9. Optimal process of PMa-WFSM.

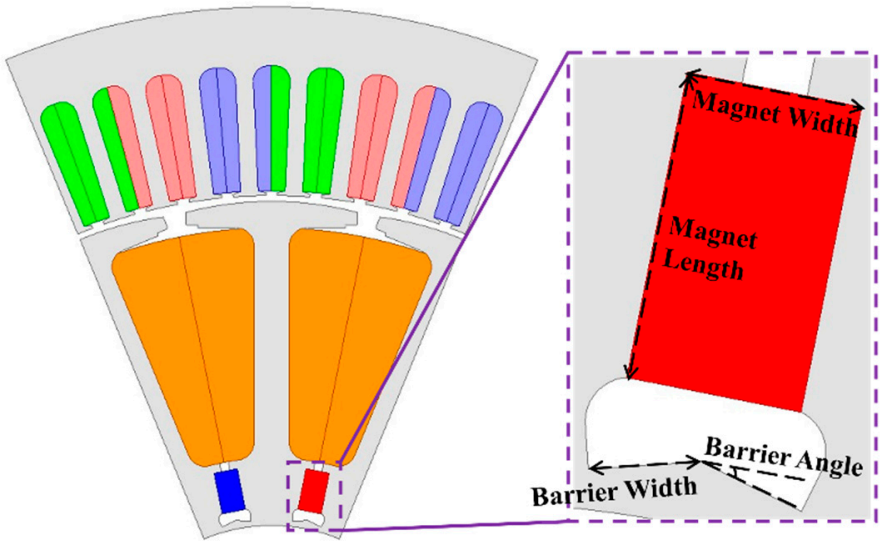

Figure 10. Design variables of PMa-WFSM.

$$nTE = 0.1 \cdot nTR \tag{7}$$

$$\text{RMSE} = \sqrt{\frac{1}{nTR}\sum_{i=1}^{nTR}[y_1(X_i) - y_2(X_i)]^2} \tag{8}$$

Utilizing the data obtained from FEM calculations, we constructed a surrogate model employing kriging interpolation to encompass the entire spectrum of variables. With this surrogate model in place, we can effectively predict output performance values across the designated range without the substantial time investment typically associated with FEM computations. Having defined our objective functions, constraints, and target functions, we allowed for the MGA to derive the optimal model. The MGA offers expedited computational time compared with normal genetic algorithms, aligning well with the goal of efficient optimization. Additionally, if applicable, we could discuss the trade-offs between conflicting objectives (e.g., maximizing efficiency while minimizing torque ripple) and how these were addressed during the optimization process. The previously set constraint conditions included an average torque of 32 Nm, a torque ripple of less than 6%, and the objective function of minimizing the cross-sectional area of the permanent magnet. Additionally, weights were assigned between the conditions. In this study, the primary objective was to match the target torque while minimizing the number of permanent magnets used. Therefore, the weight for the objective function was set to 0.8, and the remaining constraint conditions were assigned a weight of 0.2.

The iterative process for evaluating the objective function and constraints was conducted over 200 iterations, taking into account convergence criteria. This iterative process of validation and refinement not only bolstered the reliability of the training approach, laying a solid foundation for a highly reliable data-driven design optimization process. The optimized model obtained through the MGA revealed a reduction in magnet width by −49.21% and a decrease in magnet length by −4% compared with the initial model, as illustrated in Figure 11a.

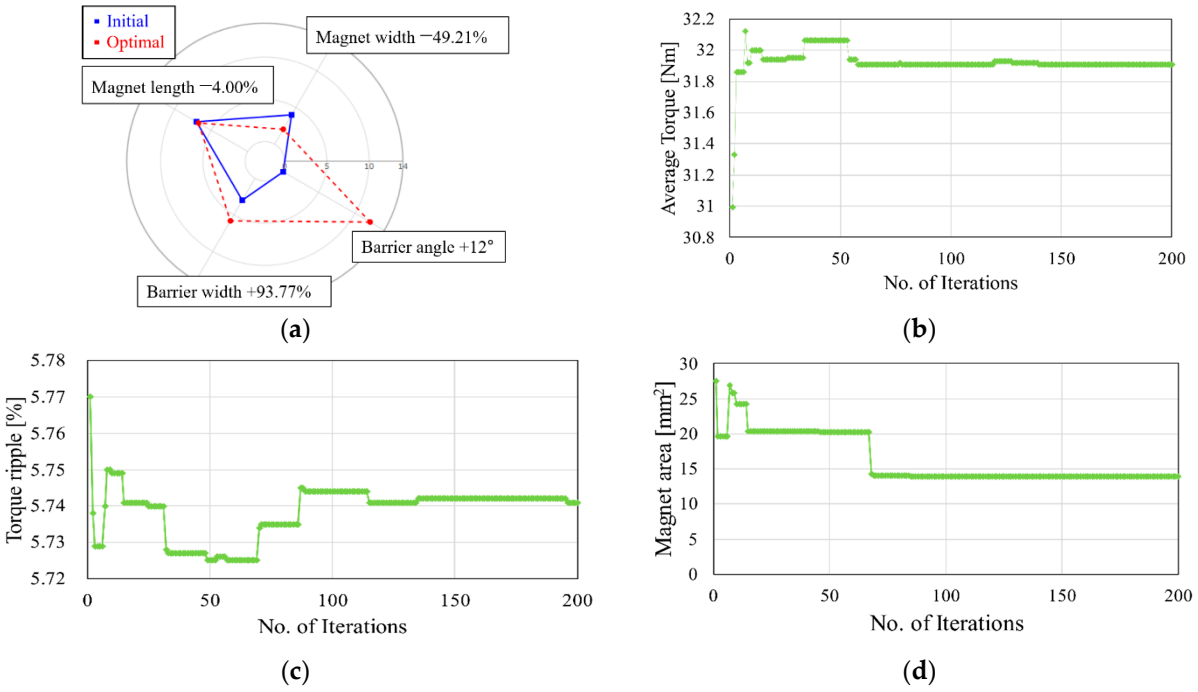

Figure 11. MGA algorithm convergence results: (**a**) variation in design variables; (**b**) target function; (**c**) constraint condition; (**d**) objective function.

Moreover, there were notable adjustments in other variables, such as a considerable increase of 93.77% in barrier width and an even more substantial increase of 12° in barrier angle. The significant increase in barrier width and angle suggests a more concentrated magnetic flux within the rotor core, potentially leading to enhanced efficiency and power density. In the initial model, the reduction in I_{dc} led to a failure to meet the target torque. The torque of the surrogate model achieved 31.91 Nm. However, the optimized model successfully achieved this target, delivering a torque of 31.61 Nm within the acceptable error range. Furthermore, there was a small improvement in torque ripple, which decreased by 0.03%. Used surrogate models serve as substitutes for intricate original models, thereby facilitating time and cost savings in the design and optimization phases of electric motors. Whereas FEM computations demand significant time, the adoption of surrogate models obviates the necessity for such computations, thereby expediting results. Additionally, surrogate models facilitate swift exploration of a wide array of design scenarios, augmenting the efficiency of the design process by providing instantaneous access to outputs for various input conditions. The comparison between the surrogate model and FEM analysis results revealed minimal discrepancies, as shown in Table 3, with torque exhibiting a mere 0.94% error and torque ripple showing only a 0.17% deviation. These results underscore the effectiveness of the optimization strategy in not only meeting the performance objectives but also in enhancing the overall performance of the WFSM.

Table 3. Comparison of results from optimal approximation model and FEM results.

	Torque	Torque Ripple
Surrogate model	31.91 Nm	5.73%
FEM model	31.61 Nm	5.72%
Error	0.94%	0.17%

5. Comparing the Characteristics WFSM and PMa-WFSM

The comparison analysis provides valuable insights into the performance disparities between the basic WFSM and the optimized PMa-WFSM, shedding light on key improvements achieved through design enhancements. Notably, the reduction in rotor current by 1.5 A_{dc} translates to a substantial decrease of 63.08 W in rotor copper loss, underscoring the efficiency gains realized with the PMa-WFSM. Furthermore, the notable decrease of 42% in rotor current density signifies enhanced heat dissipation capabilities, contributing to improved overall system reliability. Despite a marginal decrease in torque compared with the baseline, the significant reduction of 5.43% in torque ripple demonstrates the enhanced stability and smoother operation of the PMa-WFSM, with the load counter–electromotive force waveform remaining at a similar level, as shown in Figure 12. The average torque remains nearly identical, resulting in the peak and waveform of the EMF being almost the same. However, the torque ripple significantly decreases due to the increased magnetomotive force (MMF) provided by the permanent magnets. The overall output performance is enhanced with the incorporation of assisted permanent magnets compared with that of the basic WFSM shown in Table 4. The addition of permanent magnets to the basic WFSM will also increase manufacturing costs. Although it is challenging to predict the exact cost due to the unstable price of neodymium, it is estimated that the manufacturing costs will increase by approximately 10% compared with those of the basic WFSM.

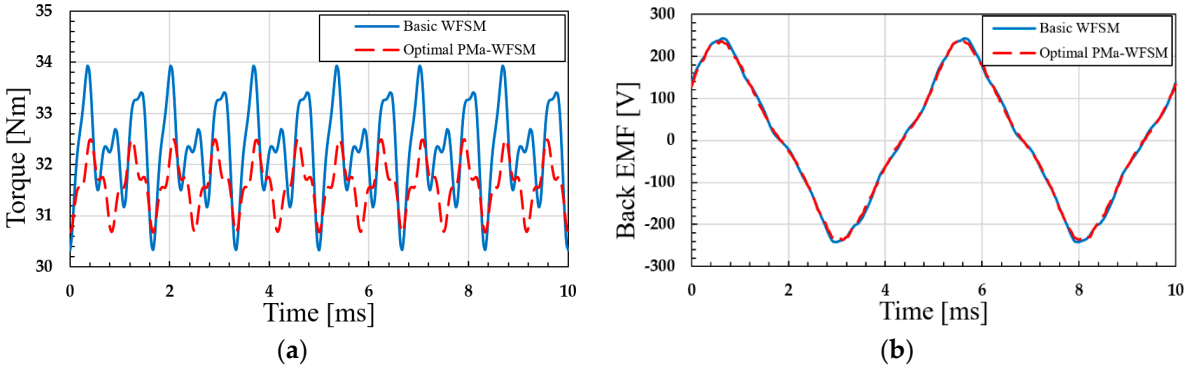

Figure 12. Comparing the output performance between WFSM and PMa-WFSM: (**a**) torque, and (**b**) load back EMF.

Table 4. Comparing the characteristics of WFSM and PMa-WFSM.

Category	WFSM	PMa-WFSM
Stator Copper loss	163.05 W	163.05 W
Stator Current density	3.85 A_{rms}/mm^2	3.85 A_{rms}/mm^2
Rotor Copper loss	123.69 W	60.61 W
Rotor Current density	3.24 A_{rms}/mm^2	2.27 A_{rms}/mm^2
Average torque	32.33 Nm	31.84 Nm
Torque ripple	11.15%	5.72%
Core loss	37.40 W	35.97 W
Efficiency	93.99%	95.07%

6. Conclusions

In this article, we aim to address the inherent limitations associated with the design of WFSM systems tailored for vehicle traction applications. Specifically, our objective is to enhance key characteristics such as high power density and efficiency, critical for traction motors operating in demanding conditions. To achieve this goal, we propose a novel variant of the WFSM, termed PMa-WFSM, which integrates assisted permanent magnets into its design architecture. The incorporation of these permanent magnets holds the potential to significantly improve performance metrics. To systematically assess the anticipated effects of permanent magnet insertion, we employ mathematical formulations and conduct equivalent circuit analyses. Through these analytical methods, we forecast the potential impact on overall system performance and validate our projections through extensive FEM simulations. The reliability and accuracy of the FEM simulation results are verified through comparison with experimental data obtained from an existing WFSM model, with the observed back EMF data error between measured data and simulation results falling within an acceptable margin of 5.06%. Furthermore, in our efforts to enhance cost-effectiveness and minimize the utilization of rare-earth materials, we undertake comprehensive optimization efforts aimed at reducing magnet usage while maintaining optimal performance levels. To streamline the analysis process, we select OLHD during the design and analysis stages, within the framework of computer experiments on DACE sampling. Additionally, we leverage the MGA as the optimization algorithm, offering computational efficiency and effectiveness. Ultimately, our optimization endeavors yield a notable enhancement in efficiency, with the system's efficiency rating improving from 93.99% to 95.07% compared with that of the existing setup. When classified according to the International Energy Efficiency class (IE), the existing WFSM falls under the IE3 category, whereas the PMa-WFSM proposed in this paper achieves an IE4 rating. This improvement not only contributes to the economic viability of the system by reducing reliance on rare-earth materials, which are commonly utilized in traction systems, but

also harnesses the inherent advantages of WFSM technology, particularly its capability for precise field current control.

Considering these advancements, we assert that the proposed PMa-WFSM emerges as a compelling alternative to normal PMSM and WFSM systems. It embodies a potent blend of heightened performance, economic viability, and operational flexibility.

Author Contributions: Conceptualization, C.-B.P. and H.-W.L.; methodology, H.-S.S. and S.-H.K.; software, H.-S.S. and S.-H.K.; validation, G.L. and Y.G.; formal analysis, H.-S.S.; investigation, H.-S.S. and S.-H.K.; writing—original draft preparation, H.-S.S.; writing—review and editing, G.L. and Y.G.; visualization, H.-W.L. and C.-B.P.; supervision, H.-W.L. and Y.G.; project administration, C.-B.P. and G.L.; funding acquisition, C.-B.P. and H.-W.L. All authors have read and agreed to the published version of the manuscript.

Funding: This work was supported by "Human Resources Program in Energy Technology" of the Korea Institute of Energy Technology Evaluation and the Korea Planning (KETEP), with granted financial resources granted by the Ministry of Trade, Industry and Energy, Republic of Korea (No. RS-2023-00243214).

Institutional Review Board Statement: Not applicable.

Informed Consent Statement: Not applicable.

Data Availability Statement: No new data were created or analyzed in this study. Data sharing is not applicable to this article.

Conflicts of Interest: The authors declare no conflict of interest.

References

1. Chai, W.; Lipo, T.A.; Kwon, B.-i. Design and Optimization of a Novel Wound Field Synchronous Machine for Torque Performance Enhancement. *Energies* **2018**, *11*, 2111. [CrossRef]
2. Jo, I.-H.; Lee, J.; Lee, H.-W.; Lee, J.-B.; Lim, J.-H.; Kim, S.-H.; Park, C.-B. A Study on MG-PMSM for High Torque Density of 45 kW–Class Tram Driving System. *Energies* **2022**, *15*, 1749. [CrossRef]
3. Li, Y.; Wang, Y.; Zhang, Z.; Li, J. Investigation and Development of the Brushless and Magnetless Wound Field Synchronous Motor Drive System for Electric Vehicle Application. *World Electr. Veh. J.* **2023**, *14*, 81. [CrossRef]
4. Petrelli, G.; Nuzzo, S.; Barater, D.; Zou, T.; Franceschini, G.; Gerada, C. Preliminary Sensitivity Analysis and Optimisation of a Wound Field Synchronous Motor for Traction Applications. In Proceedings of the 2023 AEIT International Conference on Electrical and Electronic Technologies for Automotive (AEIT AUTOMOTIVE), Modena, Italy, 17–19 July 2023; pp. 1–6. [CrossRef]
5. Lim, M.-S.; Hong, J.-P. Design of High Efficiency Wound Field Synchronous Machine with Winding Connection Change Method. *IEEE Trans. Energy Convers.* **2018**, *33*, 1978–1987. [CrossRef]
6. Kimiabeigi, M.; Widmer, J.D.; Long, R.; Gao, Y.; Goss, J.; Martin, R.; Lisle, T.; Vizan, J.S.; Michaelides, A.; Mecrow, B. High-Performance Low-Cost Electric Motor for Electric Vehicles Using Ferrite Magnets. *IEEE Trans. Ind. Electron.* **2016**, *63*, 113–122. [CrossRef]
7. Wibisono, F.I.; Asama, J. Wound Field Synchronous Motor Using a Non-Salient Pole Rotor with Distributed Winding. In Proceedings of the 2023 IEEE Energy Conversion Congress and Exposition (ECCE), Nashville, TN, USA, 29 October–2 November 2023; pp. 4030–4033. [CrossRef]
8. Morimoto, S.; Sanada, M.; Takeda, Y. Wide-speed operation of interior permanent magnet synchronous motors with high-performance current regulator. *IEEE Trans. Ind. Appl.* **1994**, *30*, 920–926. [CrossRef]
9. Zhang, W.; Fan, Y.; Zhu, Z.Q.; Wu, Z.; Hua, W.; Cheng, M. Analysis of DC Winding Induced Voltage in Wound-Rotor Synchronous Machines by Using the Air-Gap Field Modulation Principle. *World Electr. Veh. J.* **2022**, *13*, 215. [CrossRef]
10. Chai, W.; Yang, H.-M.; Xing, F.; Kwon, B.-i. Analysis and Design of a PM-Assisted Wound Rotor Synchronous Machine With Reluctance Torque Enhancement. *IEEE Trans. Ind. Electron.* **2021**, *68*, 2887–2897. [CrossRef]
11. Chae, W.C.; Kim, M.J.; Lee, K.D.; Lee, J.J.; Han, J.H.; Jung, T.C.; Lee, J. High Speed Performance Improvement of the WRSM and its Comparison with the IPMSM. *Trans. Korean Inst. Electr. Eng.* **2012**, *61*, 1595–1600. [CrossRef]
12. Yoon, K.-Y.; Lee, S.-T. Performance Improvement of Permanent-Magnet-Synchronous Motors through Rotor Shape Optimization of Marine Blowing System with High-Speed Rotation. *Energies* **2023**, *16*, 5486. [CrossRef]
13. Chattopadhyay, R.; Islam, M.S.; Boldea, I.; Husain, I. FEA Characterization of Bi-Axial Excitation Machine for Automotive Traction Applications. In Proceedings of the 2021 IEEE International Electric Machines & Drives Conference (IEMDC), Hartford, CT, USA, 17–20 May 2021; pp. 1–7. [CrossRef]
14. Hussain, A.; Baig, Z.; Toor, W.T.; Ali, U.; Idrees, M.; Shloul, T.A.; Ghadi, Y.Y.; Alkahtani, H.K. Wound Rotor Synchronous Motor as Promising Solution for Traction Applications. *Electronics* **2022**, *11*, 4116. [CrossRef]

15. Hwang, S.-W.; Sim, J.-H.; Hong, J.-P.; Lee, J.-Y. Torque Improvement of Wound Field Synchronous Motor for Electric Vehicle by PM-Assist. *IEEE Trans. Ind. Appl.* **2018**, *54*, 3252–3259. [CrossRef]
16. Xu, K.; Guo, Y.; Lei, G.; Zhu, J. Estimation of Iron Loss in Permanent Magnet Synchronous Motors Based on Particle Swarm Optimization and a Recurrent Neural Network. *Magnetism* **2023**, *3*, 327–342. [CrossRef]
17. Jo, I.H.; Lee, J.; Lee, H.W.; Lee, J.B.; Lim, J.H.; Kim, S.H.; Park, C.B. Analysis of Optimal Rotors Skew to Improve the Total Harmonic Distortion of Back Electromotive Force in MG-PMSM for Traction. *IEEE Access* **2023**, *11*, 122231–122237. [CrossRef]
18. Chu, W.Q.; Zhu, Z.Q. Average Torque Separation in Permanent Magnet Synchronous Machines Using Frozen Permeability. *IEEE Trans. Magn.* **2013**, *49*, 1202–1210. [CrossRef]
19. You, Y.-M. Optimal Design of PMSM Based on Automated Finite Element Analysis and Metamodeling. *Energies* **2019**, *12*, 4673. [CrossRef]